Solution Techniques for Large-Scale CFD Problems (ed. W.G. Habashi), Wiley & Sons (1995).

PARALLEL FINITE ELEMENT COMPUTATION OF 3D INCOMPRESSIBLE FLOWS ON MPPs

V. KALRO and T.E. TEZDUYAR

In this chapter we present numerical simulations of the Navier-Stokes equations with the stabilized finite element methods on the massively parallel CM-5 supercomputer. These computations are based on implicit methods and their implementations are based on the assumption that the mesh is unstructured. The use of matrix-free iterations eliminates the need to store element-level matrices, thus providing us with the potential to solve problems with complex 3D geometries and with more than 4,000,000 coupled nonlinear equations. The unsteady flow past a stationary cylinder is investigated at Reynolds numbers 300 and 800. Our results indicate strong three-dimensionality arising from the instability of the columnar vortices forming the Karman street. We also present results from the unsteady flow past a sphere, where intricate vortex shedding patterns are observed. Comparisons are made between computations on a semi-stuctured hexahedral mesh and an unstructured tetrahedral mesh. Finally we present a preliminary simulation of flow around high-speed trains in a tunnel. For fixed domains, we use a semi-discrete formulation, and for the trains problem we use the Deformable-Spatial-Domain/Stabilized-Space-Time(DSD/SST) formulation.

1. INTRODUCTION

In today's world of scientific computing, massively parallel processors (MPPs) have proven themselves to be superior workhorses over their traditional counterparts both in terms of large data set handling capability and shorter turn around times. Within the current framework of parallel architectures, we can distinguish between the multiple-instruction multiple-data (MIMD) and single-instruction multiple-data (SIMD) programming models. In the MIMD mode the programmer is responsible for controlling and synchronizing individual processors, whereas in the SIMD mode this task is left to the machine, and the operations are carried out on an entire array using a data-parallel programming language. The programming style and data structure utilized in either model are very different compared to traditional scalar or vector design.

The capability to use unstructured meshes or mix various types of interpolations in the same problem leads to complex communication patterns. These could be bottlenecks in the implementations and require careful consideration. Earlier work involving SIMD incompressible flow simulations related to the present work has been presented by Behr *et al.*[1] Recently Johan *et al.*[2] introduced a data-parallel implementation of the recursive spectral bisection (RSB)[3]. This domain decomposition strategy leads to the creation of element subdomains, which, reduces communication overheads and helps maintain a favorable load balance.

It is well known that incompressible finite element computations based on the standard Galerkin formulation exhibit numerical instabilities which show up as oscillations in the velocity and pressure fields. These oscillations are due to dominant advection terms[4] which can not be well represented by the central-difference-like Galerkin formulation; and due to equal-order representation for the velocity and pressure fields. The latter cause is peculiar to incompressible flows arising from

the violation of the Babuska-Brezzi condition and shows up in the form of spurious pressure oscillations. To circumvent these problems we use the streamline-upwind/Petrov-Galerkin (SUPG) and Galerkin/least-squares techniques[5,6]. These stabilized techniques introduce minimal numerical diffusion while maintaining consistency in the sense that the stabilizers are weighted residuals.

To handle moving boundaries and interfaces, we employ the Deformable-Spatial-Domain/Stabilized-Space-Time (DSD/SST) finite element formulation. This method was introduced by Tezduyar et al.[7,8] to solve incompressible flow problems involving moving boundaries and interfaces, such as free surfaces, two-liquid interfaces, and fluid-structure and fluid-particle interactions.

We discuss in this chapter our 3D incompressible flow simulations which use a massively parallel finite element implementation on the CM-5 supercomputer[9]. Our implementation is based on a SIMD, or data parallel, style of programming.

We begin by reviewing the incompressible Navier-Stokes equations in Section 2. The stabilized variational formulation written in terms of velocity and pressure variables is presented in Section 3. Brief remarks concerning implementation on massively parallel machines comprise Section 4. The methods described in the previous sections are applied in Section 5 to solve 3D flows past cylinders and spheres and to simulate flow around high-speed trains in a tunnel. Finally we summarize the performance of our computations in Section 6.

2. THE GOVERNING EQUATIONS

Let $\Omega_t \subset \mathbb{R}^{n_{sd}}$ and $(0,T)$ be the spatial and temporal domains respectively, where n_{sd} is the number of space dimensions, and let Γ_t denote the boundary of Ω_t. The subscript "t" implies the time-dependence of the spatial domain. The spatial and temporal coordinates are denoted by $\mathbf{x}$ and t. The Navier-Stokes equations governing incompressible fluid flow are

$$\rho(\frac{\partial \mathbf{u}}{\partial t} + \mathbf{u}\cdot\nabla\mathbf{u} - \mathbf{f}) - \nabla\cdot\boldsymbol{\sigma} = 0 \qquad \text{on } \Omega_t \text{ for } (0,T), \tag{1}$$

$$\nabla\cdot\mathbf{u} = 0 \qquad \text{on } \Omega_t \text{ for } (0,T). \tag{2}$$

Here ρ, $\mathbf{u}$, $\mathbf{f}$ and $\boldsymbol{\sigma}$ are the density, velocity, body force and the stress tensor, respectively. The stress tensor is written as the sum of its isotropic and deviatoric parts:

$$\boldsymbol{\sigma} = -p\mathbf{I} + \mathbf{T}, \quad \mathbf{T} = 2\mu\boldsymbol{\varepsilon}(\mathbf{u}), \quad \boldsymbol{\varepsilon}(\mathbf{u}) = \frac{1}{2}((\nabla\mathbf{u}) + (\nabla\mathbf{u})^T), \tag{3}$$

where p and μ are the pressure and viscosity. Both the Dirichlet and Neumann-type boundary conditions are accounted for, represented as

$$\mathbf{u} = \mathbf{g} \text{ on } (\Gamma_t)_g, \quad \mathbf{n}\cdot\boldsymbol{\sigma} = \mathbf{h} \text{ on } (\Gamma_t)_h, \tag{4}$$

where $(\Gamma_t)_g$ and $(\Gamma_t)_h$ are complementary subsets of the boundary Γ_t. The initial condition on the velocity is specified on Ω_0:

$$\mathbf{u}(\mathbf{x},0) = \mathbf{u}_0 \quad \text{on } \Omega_0, \tag{5}$$

where $\mathbf{u}_0$ is divergence free.

3. FINITE ELEMENT FORMULATIONS

3.1 Fixed Domains - Semi-Discrete Formulation

Consider a finite element discretization of Ω (the subscript t has been dropped for the fixed domain) into subdomains Ω^e, $e = 1, 2, ..., n_{el}$, where n_{el} is the number of elements. Based on this discretization, for velocity and pressure we define the finite element trial function spaces $\mathcal{S}_{\mathbf{u}}^h$ and $\mathcal{S}_p^h$, and weighting function spaces $\mathcal{V}_{\mathbf{u}}^h$ and $\mathcal{V}_p^h$. These function spaces are selected, by taking the Dirichlet boundary conditions into account, as subsets of $[\mathbf{H}^{1h}(\Omega)]^{n_{sd}}$ and $\mathbf{H}^{1h}(\Omega)$, where $\mathbf{H}^{1h}(\Omega)$ is the finite-dimensional function space over Ω. The stabilized finite element formulation of Eq. (1)-(2) is written as follows: find $\mathbf{u}^h \in \mathcal{S}_{\mathbf{u}}^h$ and $p^h \in \mathcal{S}_p^h$ such that $\forall \mathbf{w}^h \in \mathcal{V}_{\mathbf{u}}^h$, $q^h \in \mathcal{V}_p^h$

$$\int_\Omega \mathbf{w}^h \cdot \rho \left(\frac{\partial \mathbf{u}^h}{\partial t} + \mathbf{u}^h \cdot \nabla \mathbf{u}^h - \mathbf{f} \right) d\Omega + \int_\Omega \boldsymbol{\varepsilon}(\mathbf{w}^h) : \boldsymbol{\sigma}(p^h, \mathbf{u}^h) d\Omega + \int_\Omega q^h \nabla \cdot \mathbf{u}^h d\Omega$$
$$+ \sum_{e=1}^{n_{el}} \int_{\Omega^e} \frac{1}{\rho} \left(\tau_{\text{SUPG}} \rho \mathbf{u}^h \cdot \nabla \mathbf{w}^h + \tau_{\text{PSPG}} \nabla q^h \right) \cdot$$
$$\left[\rho \left(\frac{\partial \mathbf{u}^h}{\partial t} + \mathbf{u}^h \cdot \nabla \mathbf{u}^h - \mathbf{f} \right) - \nabla \cdot \boldsymbol{\sigma}(p^h, \mathbf{u}^h) \right] d\Omega^e$$
$$+ \sum_{e=1}^{n_{el}} \int_{\Omega^e} \delta \nabla \cdot \mathbf{w}^h \rho \nabla \cdot \mathbf{u}^h d\Omega^e = \int_{\Gamma_h} \mathbf{w}^h \cdot \mathbf{h}^h d\Gamma \quad (6)$$

Remarks

1. In the variational formulation given by Eq. (6), the first three terms and the right-hand-side constitute the Galerkin formulation of the problem.
2. The first series of element-level integrals are the SUPG and PSPG stabilization terms added to the variational formulations. In the current formulation τ_{PSPG} is the same as τ_{SUPG} and is given as

$$\tau = \left(\left(\frac{2 \parallel \mathbf{u}^h \parallel}{h} \right)^2 + \left(\frac{4\nu}{h^2} \right)^2 \right)^{-\frac{1}{2}}. \quad (7)$$

3. The second series of element-level integrals are added to the formulation for numerical stability at high Reynolds numbers. This is a least-squares term based on the continuity equation. The coefficient δ is defined as

$$\delta = \frac{h}{2} \parallel \mathbf{u}^h \parallel z, \quad (8)$$

where

$$z = \begin{cases} \left(\frac{Re_u}{3}\right) & Re_u \leq 3 \\ 1 & Re_u > 3 \end{cases},$$

and Re_u is the cell Reynolds number.

4. Both stabilization terms are weighted residuals, and therefore maintain the consistency of the formulation.

3.2 Deforming Domains – Space-Time Formulation

In order to construct the finite element function spaces for the space-time method, we partition the time interval $(0,T)$ into subintervals $I_n = (t_n, t_{n+1})$, where t_n and t_{n+1} belong to an ordered series of time levels $0 = t_0 < t_1 < \cdots < t_N = T$. Let $\Omega_n = \Omega_{t_n}$ and $\Gamma_n = \Gamma_{t_n}$. We define the space-time slab Q_n as the domain enclosed by the surfaces Ω_n, Ω_{n+1}, and P_n, where P_n is the surface described by the boundary Γ_t as t traverses I_n. As it is the case with Γ_t, surface P_n is decomposed into $(P_n)_g$ and $(P_n)_h$ with respect to the type of boundary condition (Dirichlet or Neumann) being imposed. For each space-time slab we define the corresponding finite element function spaces $(\mathcal{S}^h_{\mathbf{u}})_n$, $(\mathcal{V}^h_{\mathbf{u}})_n$, $(\mathcal{S}^h_p)_n$, and $(\mathcal{V}^h_p)_n$. Over the element domain, this space is formed by using first-order polynomials in space and time. Globally, the interpolation functions are continuous in space but discontinuous in time.

The stabilized space-time formulation for deforming domains is then written as follows: given $(\mathbf{u}^h)_{n^-}$, find $\mathbf{u}^h \in (\mathcal{S}^h_{\mathbf{u}})_n$ and $p^h \in (\mathcal{S}^h_p)_n$ such that $\forall \mathbf{w}^h \in (\mathcal{V}^h_{\mathbf{u}})_n$, $q^h \in (\mathcal{V}^h_p)_n$

$$\int_{Q_n} \mathbf{w}^h \cdot \rho \left(\frac{\partial \mathbf{u}^h}{\partial t} + \mathbf{u}^h \cdot \boldsymbol{\nabla} \mathbf{u}^h - \mathbf{f} \right) d\Omega + \int_{Q_n} \boldsymbol{\varepsilon}(\mathbf{w}^h) : \boldsymbol{\sigma}(p^h, \mathbf{u}^h) dQ + \int_{Q_n} q^h \boldsymbol{\nabla} \cdot \mathbf{u}^h dQ$$
$$+ \sum_{e=1}^{n_{el}} \int_{Q_n^e} \frac{1}{\rho} \tau \left[\rho \left(\frac{\partial \mathbf{w}^h}{\partial t} + \mathbf{u}^h \cdot \boldsymbol{\nabla} \mathbf{w}^h \right) - \boldsymbol{\nabla} \cdot \boldsymbol{\sigma}(q^h, \mathbf{w}^h) \right] \cdot$$
$$\left[\rho \left(\frac{\partial \mathbf{u}^h}{\partial t} + \mathbf{u}^h \cdot \boldsymbol{\nabla} \mathbf{u}^h - \mathbf{f} \right) - \boldsymbol{\nabla} \cdot \boldsymbol{\sigma}(p^h, \mathbf{u}^h) \right] dQ$$
$$+ \sum_{e=1}^{n_{el}} \int_{Q_n^e} \delta \boldsymbol{\nabla} \cdot \mathbf{w}^h \rho \boldsymbol{\nabla} \cdot \mathbf{u}^h dQ + \int_{\Omega_n} (\mathbf{w}^h)_n^+ \cdot \rho \left((\mathbf{u}^h)_n^+ - (\mathbf{u}^h)_n^- \right) d\Omega = \int_{(P_n)_h} \mathbf{w}^h \cdot \mathbf{h}^h dP \quad (9)$$

This process is applied sequentially to all the space-time slabs $Q_1, Q_2, \ldots, Q_{N-1}$. In the variational formulation given by Eq. (9), the following notation is being used:

$$(\mathbf{u}^h)_n^{\pm} = \lim_{\varepsilon \to 0} \mathbf{u}(t_n \pm \varepsilon), \quad (10)$$

$$\int_{Q_n} (\ldots) dQ = \int_{I_n} \int_{\Omega_n} (\ldots) d\Omega dt, \quad (11)$$

$$\int_{P_n} (\ldots) dP = \int_{I_n} \int_{\Gamma_n} (\ldots) d\Gamma dt. \tag{12}$$

The computations start with

$$(\mathbf{u}^h)_0^- = \mathbf{u}_0, \tag{13}$$

where $\mathbf{u}_0$ is divergence free.

Remarks

5. The fourth term in Eq. (9) is a least-squares term based on the momentum equation, and plays the roles of both the PSPG and the SUPG operators.
6. The sixth term enforces weak continuity of the velocity field across the space-time slabs.

4. MASSIVELY PARALLEL IMPLEMENTATIONS

The coupled nonlinear equation systems arising from the finite element formulations described in section 3 are solved iteratively using diagonal preconditioners and the GMRES[10] technique. For problems with large memory demands, matrix-free[2] versions of these iterative techniques are used.

These procedures have been implemented on the massively parallel CM-200 and CM-5 supercomputers. The highlights of the current implementations are listed below.

1. Use of data structures which avoid interprocessor communication of data.
2. Distribution of data across processors so as to maximize and exploit data locality.
3. Use of efficient gather and scatter algorithms with favorable ratios of on-processor to off-processor data transfers.
4. Favorable load balancing and scaling properties.

For details of the implementation the reader is referred to Kennedy *et al.*[9]

5. NUMERICAL SIMULATIONS

5.1 3D Flow Past a Sphere at Re = 400

Wakes behind spheres are often encountered in engineering applications and have attracted considerable amount of experimental investigation. At low Reynolds numbers an axisymmetric steady flow, which separates at $Re \approx 24$, is observed. Experiments show that at Reynolds number in the range of 120 - 300, the axisymmetric flow loses its stability to a non-axisymmetric and unsteady flow. At $Re \approx 300$ laminar hairpin vortices are periodically shed with uniform strength and frequency. The Strouhal number corresponding to the shedding frequency is in the range of 0.120 - 0.160. At higher Reynolds numbers (> 800) the vortices become turbulent and two modes of shedding have been observed in experiments[11]. The lower mode

corresponds to the instability of the separating shear layer, and the higher mode to the large-scale instability of the wake structure itself.

We used both hexahedral and tetrahedral meshes to simulate the flow field. The hexahedral mesh consists of 160,006 nodes and 150,976 elements (see Fig. 1), and results in 615,703 unknowns. The domain extends from 15 units upstream to 30 units downstream. The radius of the sphere is taken as the unit length. The outer boundary has a square cross section with each side being 14 units long. The tetrahedral mesh consists of 85,020 nodes and 532,147 elements (see Fig. 2), and results in 332,206 unknowns. The domain extends from 15 units upstream to 30 units downstream. The outer boundary has a circular cross-section with radius 7 units. The boundary conditions consist of uniform inflow velocity, zero-normal-velocity (or zero-crossflow-velocity) and zero-shear-stress at the lateral boundaries, a traction-free outflow boundary, and no-slip on the sphere.

With the hexahedral mesh we tried both the zero-normal-velocity and zero-crossflow conditions at the lateral boundaries. In both cases we observed hairpin vortices shed periodically with uniform frequency and strength. The shedding occurs in a fixed plane, and we believe this is due to the bias introduced by the mesh as it offers minimum resistance along the diagonals of the crossflow section. Both regular and irregular shedding modes were observed in experiments, where the plane of shedding oscillates intermittently and in a rather random fashion about a streamwise axis. In our computations the Strouhal number corresponding to the shedding frequency is ~ 0.125. Since the shedding occurs in a fixed plane, the drag oscillates at a frequency twice that of the side forces (see Fig. 3). This is similar to vortex shedding observed in cylinder wakes.

With the tetrahedral mesh we imposed zero-crossflow conditions together with zero-shear at the the lateral boundaries. We observe that hairpin vortices are shed periodically, but no longer in a fixed plane. We also observe that the drag and lift oscillate with the same frequency (see Fig. 4). The Strouhal number is ~ 0.134 and is in good agreement with experiments. Visualization of the magnitude of the vorticity in the flow field indicates that there is a rotating separation process. This rules out the possibility of vortices being shed in the form of rings. Also, the vortices cannot form helical structures since these would give rise to a net flux of vorticity through planes perpendicular to the streamwise direction (and under the assumption that the free-stream is irrotational this violates Kelvin's circulation theorem)[12]. In fact the separated vortex sheet aft of the sphere undergoes involution[13]. Two parallel vortex trails emanate from the involuted sheet forming a loop and carry vorticity to the mainstream. These loops (which bear vorticity in an opposite sense to each other) stretch downstream and break away periodically (see Fig. 5). Since vortex tubes cannot terminate abruptly in the flow field (vorticity is a solenoidal quantity by definition), downstream of the sphere these loops are attached to each other.

5.2 3D Flow Past a Circular Cylinder

The wake behind a cylinder is a fundamental problem involving smooth bodies of finite thickness and has been the focus of extensive studies, both experimentally and numerically. Until recently most numerical simulations have been restricted to 2D due to lack of computational power, whereas experiments indicate the presence of strong three-dimensionality above $Re = 200$.

At low Reynolds numbers one observes symmetric attached eddies aft of the cylinder. At $Re = 40$, the wake becomes unstable and begins to oscillate. These oscillations roll up into discrete vortices which are periodically shed when $Re > 60$. This uniformly spaced trail of vortices is referred to as the Karman vortex street. The Strouhal number corresponding to the shedding frequency is ~ 0.200. At $Re > 200$ the vortex street becomes unstable to perturbations in the axial direction and this marks the onset of three-dimensionality. Computations at $Re = 300$ and 800 were performed on a mesh of hexahedral elements (see Fig. 6,7). The diameter of the cylinder is 2 units and the length is 8 units (this length was chosen after some trials so as to capture a few wavelengths in the axial direction). The mesh extends 15 units upstream, 60 units downstream, and 30 units in the crossflow direction. The mesh consists of 186,240 elements (4656 elements in a 2D section) and 197,948 nodes, and results in 760,107 equations. The boundary conditions consists of uniform inflow velocity, zero-normal-velocity and zero-shear-stress at the lateral boundaries, traction-free conditions at the outflow boundary, and no-slip on the cylinder.

5.2.1 Flow at $Re = 300$ This computation was advanced in time until it was observed that the spatially-averaged aerodynamic coefficients reached a periodic state (see Fig. 8).

A Karman vortex street is observed in this periodic state, and the corresponding Strouhal number is ~ 0.205. To get a measure of the three dimensionality, we trace the time histories of the velocity and pressure at 2.85 units downstream of the cylinder along the centerline (see Fig. 10). Note that the 'v' component of velocity has a frequency half that of 'u' which is due to the alternating signs of vortices (this is also the reason why the lift has double the period of the drag). Furthermore the power spectra show the existence of two dominant frequencies for 'w'; one of them corresponding to the shedding frequency and the other twice that. Visualization of the vorticity magnitude reveals the presence of columnar vortices with their axes aligned with that of the cylinder (see Fig. 11). In the near-wake these exhibit sinusoidal variations in the axial direction which appear to be fairly regular. With the present mesh we capture 4 - 5 wavelengths. Further downstream these variations grow significantly and make the vortices bend, this, along with diffusion, cause the vortices to mingle and lose their individual nature.

5.2.2 Flow at $Re = 800$ The drag and lift time-histories for this case are shown in Fig. 9. The three dimensionality gets stronger with increasing Reynolds number. This is indicated by the 'w' component of velocity (see Fig. 12). The power spectra

of 'w' indicates the existence of multiple peaks. However the dominant frequency in the spectra still corresponds to the vortex shedding frequency. We also observe the presence of a peak at a frequency half that of the dominant frequency. The axial variations along the vortices are more prominent and the vortices bend and begin to merge in the near-wake (see Fig. 13).

5.3 Flow Around High-speed Trains in a Tunnel

Aerodynamics play a crucial role in the design and development of high-speed trains, from the point of view of cost effectiveness, safety, comfort, and minimal impact on the environment, amongst many other factors. Trains passing each other, especially in tunnels, create pressure transients which may threaten the structural integrity of the trains, besides causing some discomfort to the passengers.

We use the DSD/SST formulation to carry out a preliminary simulation. The mesh used is rather coarse for a 3D problem with intricate geometries and therefore we attach to the results only a qualitative significance. The mesh consists of 51,584 hexahedral elements and 117,214 space-time nodes, and results in 434,576 equations. To accommodate the motion of the trains we have developed a special algebraic mesh moving and remeshing scheme where elements are transplanted from regions fore of the trains to regions aft of the trains when they become overtly distorted. The total number of nodes and elements remains fixed during the simulation.

Boundary conditions consists of no-slip on the trains, traction-free conditions at the tunnel entrances and zero-normal-velocity and zero-shear-stress on the tunnel walls. At the start of the simulation the trains are at rest near the tunnel entrances and accelerate (during $t \in (0.0, 1.0)$) to 100 m/s, which is the speed at which they pass each other (during $t \in (2.0, 3.0)$).

We observe that as the trains gain speed, high-pressure regions develop at the front end and low-pressure regions at the rear. An estimate of the pressure coefficient at the front end when the trains reach their peak speeds is provided by the Bernoulli equation (for steady inviscid flow). This estimate gives us a value of 1.0. As the trains near each other the pressure in their fronts increases, and starts dropping as they pass each other. The pressure drop is maximum at the rear. After the trains have passed each other the pressure starts recovering again. The pressure coefficient at the nose becomes close to 1.0 (this is close to the estimate mentioned earlier because the flow field is now approximately steady and close to the conditions under which the estimation is more valid). From this simulation we estimate a pressure drop of 12 kPa ($Cp = 2.0$, where Cp is based on peak speed of one train) at the rear end (see Fig. 14). Experiments[14] have shown a pressure drop of 14 kPa to 16 kPa. It is, however, important to note that the pressure changes depend very strongly on the aerodynamic shape of the trains (for which we have a very simple model). Also since the relative Mach number during the passing is close to 0.6, compressible effects could be important.

The Reynolds number corresponding to the peak speed and length of the train is $\sim$ 10,000,000. Therefore we also carried out a simulation involving a simple tur-

	PN	MESH 1	MESH 2	MESH 3	MESH 4
Number of Nodes		160,006	216,248	468,998	929,808
Number of Elements		150,976	205,600	452,000	904,384
Number of Equations		615,703	836,999	1,828,319	3,644,127
Communication(%)	256	24.18	23.05	23.70	-
	512	24.17	25.65	22.50	24.01
Computation Speed(Gflops)	256	3.72	3.75	4.44	-
	512	6.30	7.02	8.27	9.11
Cost/iteration(secs)	256	3.39	4.58	8.50	-
	512	1.98	2.46	4.59	8.63
Cost/iteration/node(μsecs)	256	21.17	21.18	18.02	-
	512	12.37	11.40	9.78	9.28

TABLE 1: Performance benchmarking of incompressible solver on CM-5 using hexahedral sphere mesh.

bulence model. Here the Reynolds stresses are modeled by a modified Smagorinsky model as described in Kato and Ikegawa[15]. This algebraic modeling results in the addition of locally defined turbulent viscosity given as

$$\nu_t = C_s h^2 \sqrt{2\boldsymbol{\varepsilon}(\mathbf{u}) : \boldsymbol{\varepsilon}(\mathbf{u})}, \tag{14}$$

where $\boldsymbol{\varepsilon}(\mathbf{u})$ is the strain rate tensor, $C_s = 0.0225$, and h is the element length.

Fig. 15 shows the time history of the pressure coefficients at the front, back, and inner side of one of the trains with this simple turbulence model. Fig. 16 shows the surface mesh and pressure field at three different instants in the domain. From Fig. 15 we note that the pressure changes predicted by this model are high (especially at the front end), and this is indicative of the need for a more sophisticated turbulence model.

6. CONCLUSIONS

We used the sphere problem with hexahedral meshes to benchmark the speed, efficiency and scalability of our computations on the CM-5. We used the $2 \times 2 \times 2$ Gaussian quadrature, and the nonlinear systems of equations were solved with matrix-free iterations. The Krylov subspace dimension in the GMRES update technique was set to 10.

The reported computation rates take into account only the floating point operations involved in residual formation and in the GMRES operations, and communication costs involved in transferring data between element and equation levels.

Table 1 gives the summary of the performance in computations on the CM-5. We note that, provided the subgrid length for meshes is large enough,

- for a given partition size, solution time increases linearly with the problem size;

- for a given mesh we achieve close to linear speed-up as partition size increases, and
- communication costs are in the range 22% to 26%.

These results establish the scalable performance of our finite element solver and the CM-5 machine.

On this computational platform, with our semi-discrete formulation we were able to capture the strongly 3D character of the wake of the circular cylinder. We were also able to bring out the vortex shedding mechanism in the wake of a sphere. We obtained preliminary results using the DSD/SST technique to simulate flow around high-speed trains passing each other in a tunnel. We have made exclusive use of diagonal preconditioners for the solution of the linear systems involved in Newton-Raphson solution of the coupled nonlinear equations. However, we stress the need for efficient parallel implementation of sophisticated preconditioners to accelerate convergence.

REFERENCES

1. M. Behr, A. Johnson, J. Kennedy, S. Mittal and T.E. Tezduyar, *Computation of incompressible flows with implicit finite element implementations on the Connection Machine*, Computer Methods in Applied Mechanics and Engineering, **108** (1993) 99–118.
2. Z. Johan, *Data Parallel Finite Element Techniques for Large-Scale Computational Fluid Dynamics*, Ph.D. thesis, Department of Mechanical Engineering, Stanford University, 1992.
3. A. Pothen, H.D. Simon and L. Wang, *Spectral nested dissection*, Technical Report RNR-92-003, NASA Ames Research Center, Moffett Field, January 1992.
4. T.J.R. Hughes and A.N. Brooks, *A multi-dimensional upwind scheme with no crosswind diffusion*, in T.J.R. Hughes (ed.), Finite Element Methods for Convection Dominated Flows, AMD-**34**, 19–35, ASME Press, 1979.
5. T.E. Tezduyar, *Stabilized finite element formulations for incompressible flow computations*, Advances in Applied Mechanics, **28** (1991) 1–44. ⟵ (1992)
6. T.E. Tezduyar, S. Mittal, S.E. Ray and R. Shih, *Incompressible flow computations with stabilized bilinear and linear equal-order-interpolation velocity-pressure elements*, Computer Methods in Applied Mechanics and Engineering, **95** (1992) 221–242.
7. T.E. Tezduyar, M. Behr and J. Liou, *A new strategy for finite element computations involving moving boundaries and interfaces – the deforming-spatial-domain/space-time procedure: I. The concept and the preliminary tests*, *Computer Methods in Applied Mechanics and Engineering*, **94** (1992) 339–351.
8. T.E. Tezduyar, M. Behr, S. Mittal and J. Liou, *A new strategy for finite element computations involving moving boundaries and interfaces – the deforming-spatial-domain/space-time procedure: II. Computation of free-surface flows, two-liquid flows and flows with drifting cylinders*, Computer Methods in Applied Mechanics and Engineering, **94** (1992) 353–371.
9. J.G. Kennedy, M. Behr, V. Kalro and T.E. Tezduyar, *Implementation of implicit finite element methods for incompressible flows on the CM-5*, ~~to appear in~~ Computer Methods in Applied Mechanics and Engineering, ~~(1995).~~ **119** (1994) 95-111.
10. Y. Saad and M. Schultz, *GMRES: A generalized minimal residual algorithm for solving nonsymmetric linear systems*, SIAM Journal of Scientific and Statistical Computing, **7** (1986) 856–869.
11. H. Sakamoto and H. Haniu, *A study of vortex shedding from spheres in a uniform flow.*, Journal of Fluids Engineering, **112** (1990) 386–392.
12. E. Achenbach, *Vortex shedding from spheres*, Journal of Fluid Mechanics, **62** (2) (1974) 209–221.

13. R.H. Magarvey and C.S. Maclatchy, *Vortices in sphere wakes.*, Canadian Journal of Physics, **43** (1965) 1649–1656.
14. M. Kaiho, 1994, Personal Communication.
15. C. Kato and M. Ikegawa, *Large eddy simulation of unsteady turbulent wake of a circular cylinder using the finite element method*, in I. Celik, T. Kobayashi, K.N. Ghia and J. Kurokawa, (eds.), Advances in Numerical Simulation of Turbulent Flows, ASME FED-117, ASME Press, (1991) 49–56.

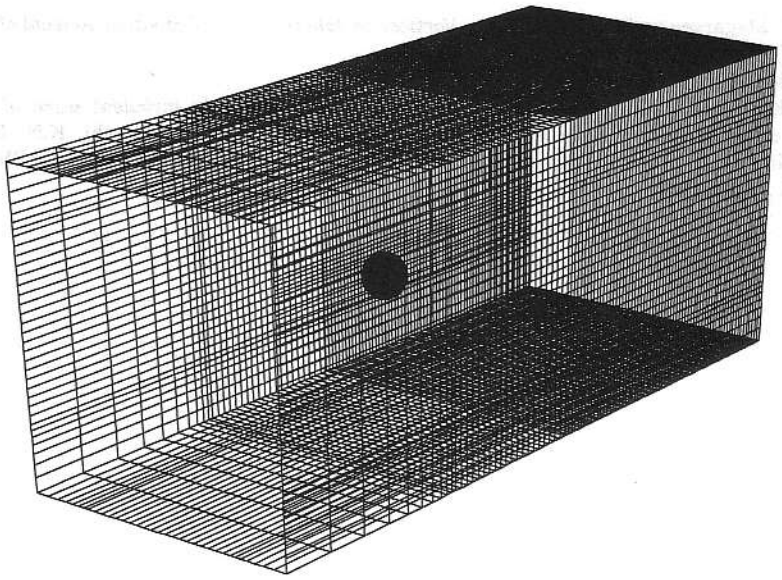

FIGURE 1: Hexahedral mesh used for computing flow past a sphere (160,006 nodes and 150,976 elements).

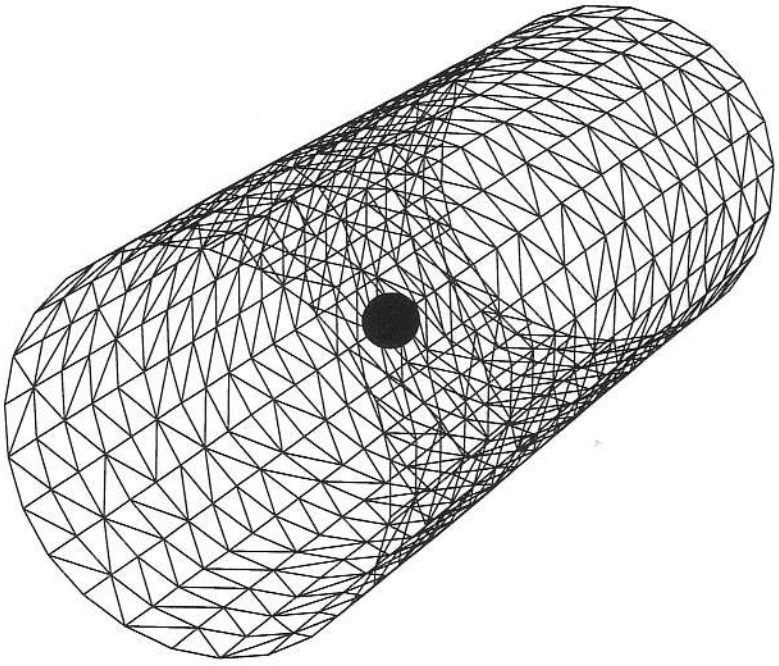

FIGURE 2: Tetrahedral mesh used for computing flow past a sphere (85,020 nodes and 532,147 elements).

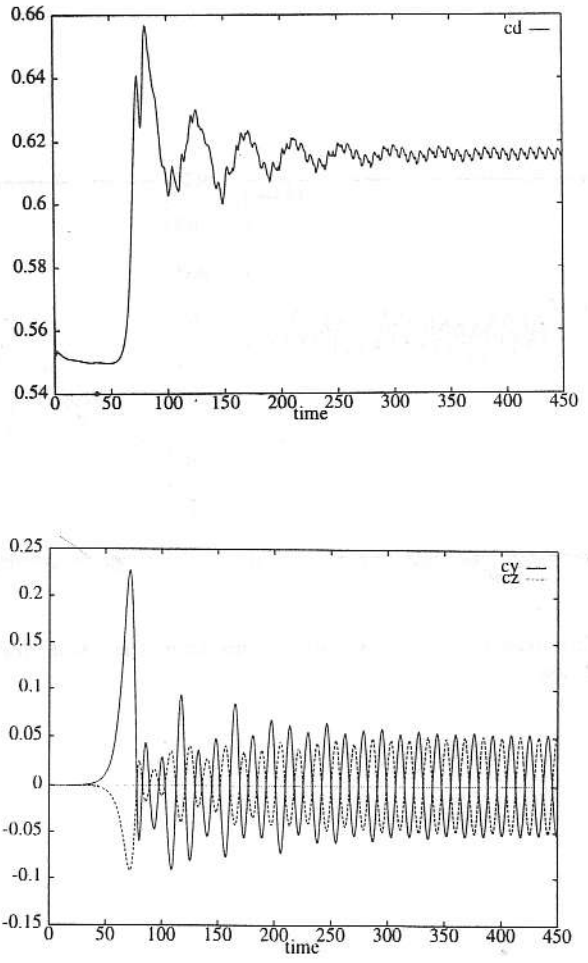

FIGURE 3: Flow past a sphere at Re=400, computed on the hexahedral mesh with slip condition at lateral boundaries. Time history of the force coefficients.

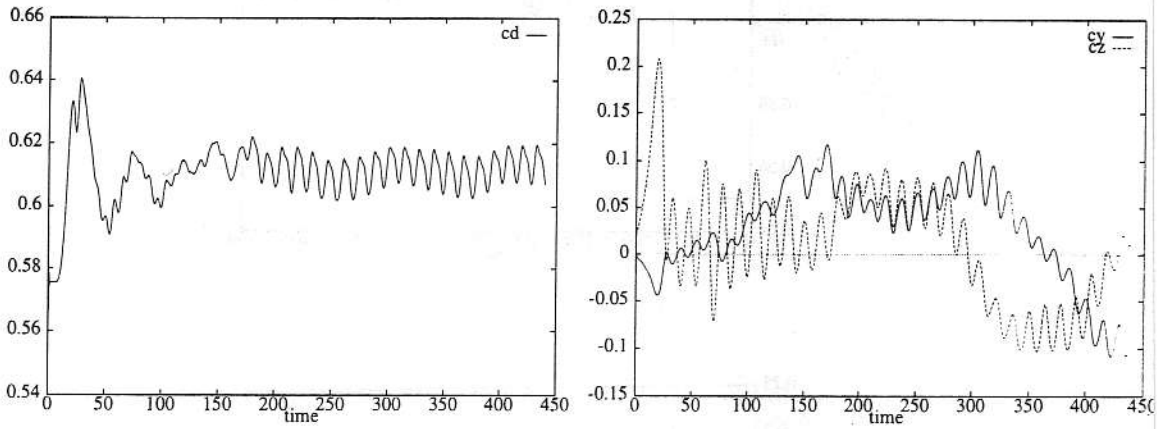

FIGURE 4: Flow past a sphere at Re=400, computed on the tetrahedral mesh. Time history of the force coefficients.

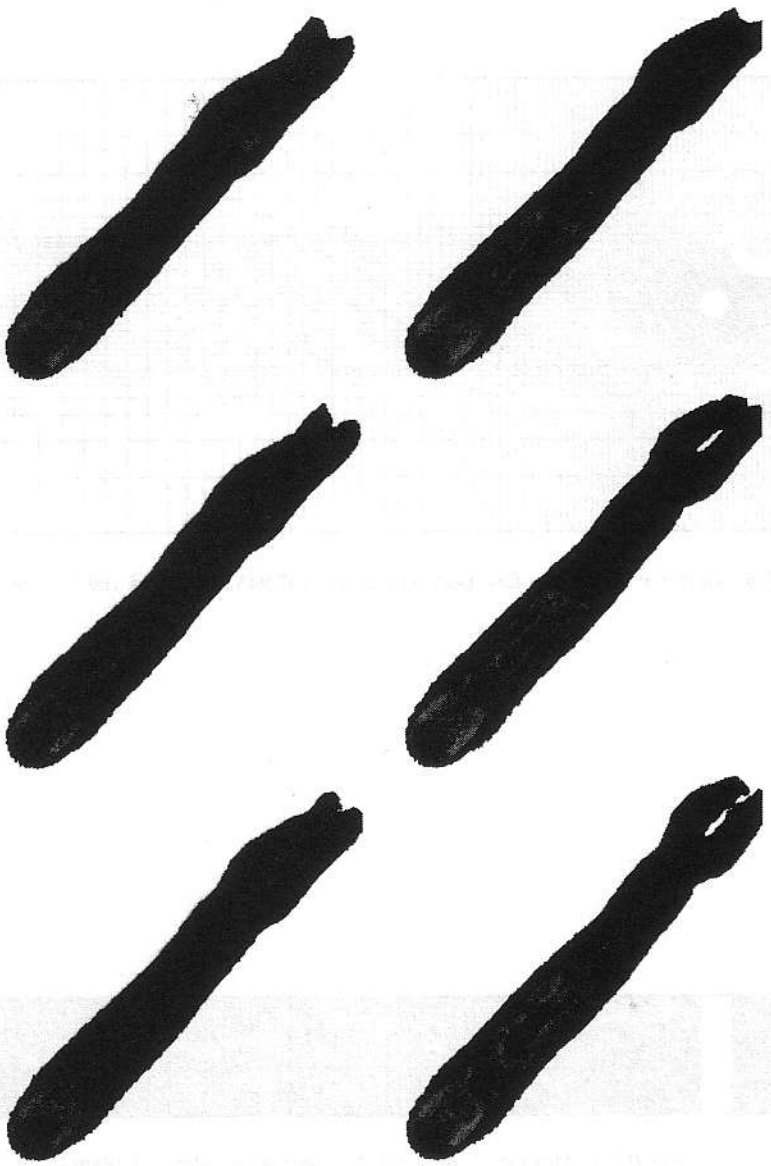

FIGURE 5: Flow past a sphere at Re=400, computed on the tetrahedral mesh. Magnitude of the vorticity at different instants highlights the mechanism through which vortex tubes develop, stretch and finally break away (frames 1, 2, 3 on the left and 4 ,5, 6 on the right).

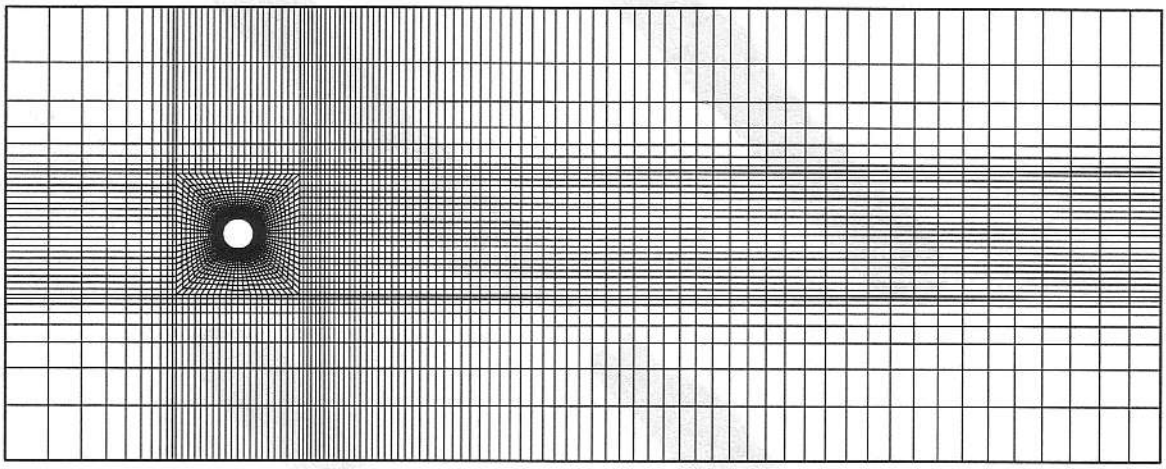

FIGURE 6: Mesh for computing flow past a cylinder (197,948 nodes and 186,240 elements) (x-y plane).

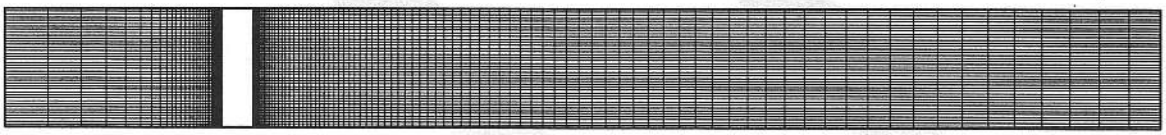

FIGURE 7: Mesh for computing flow past a cylinder (x-z plane).

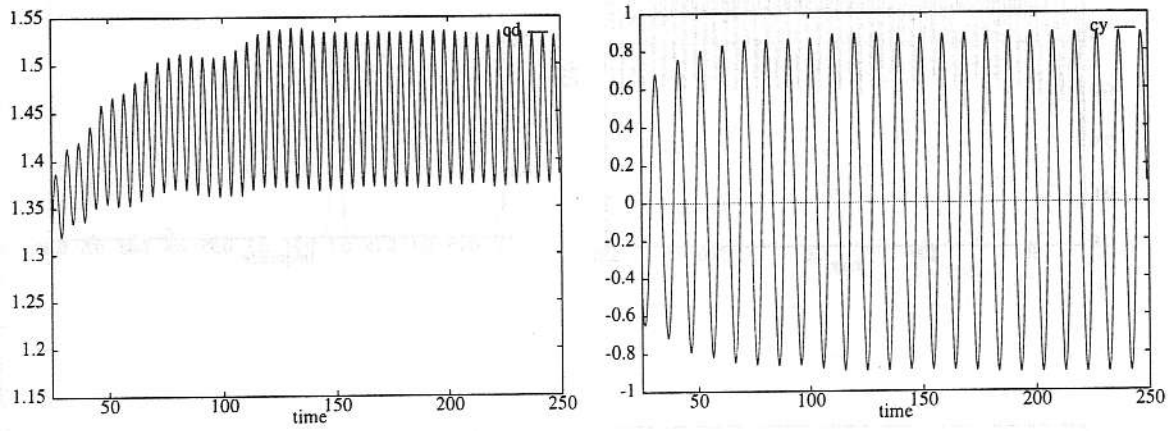

FIGURE 8: Flow past a cylinder at Re=300. Time history of the force coefficients.

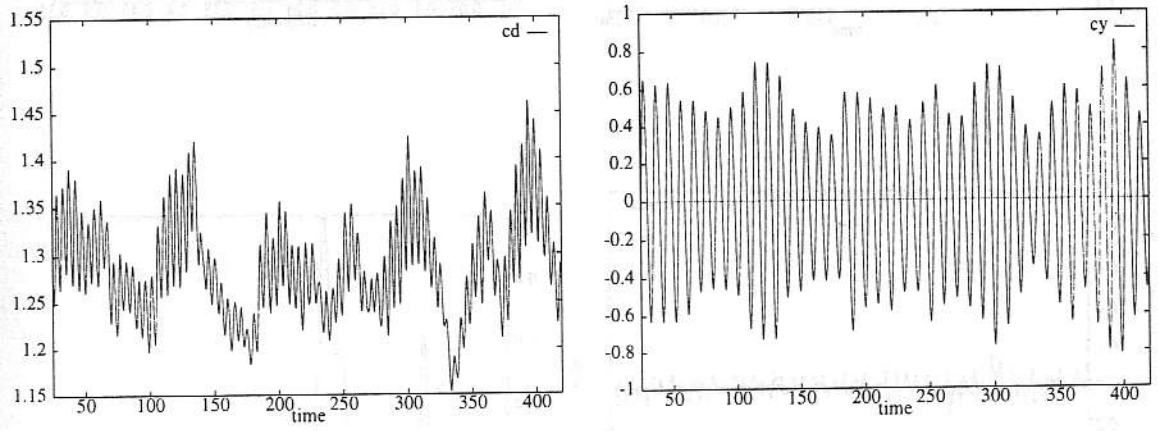

FIGURE 9: Flow past a cylinder at Re=800. Time history of the force coefficients.

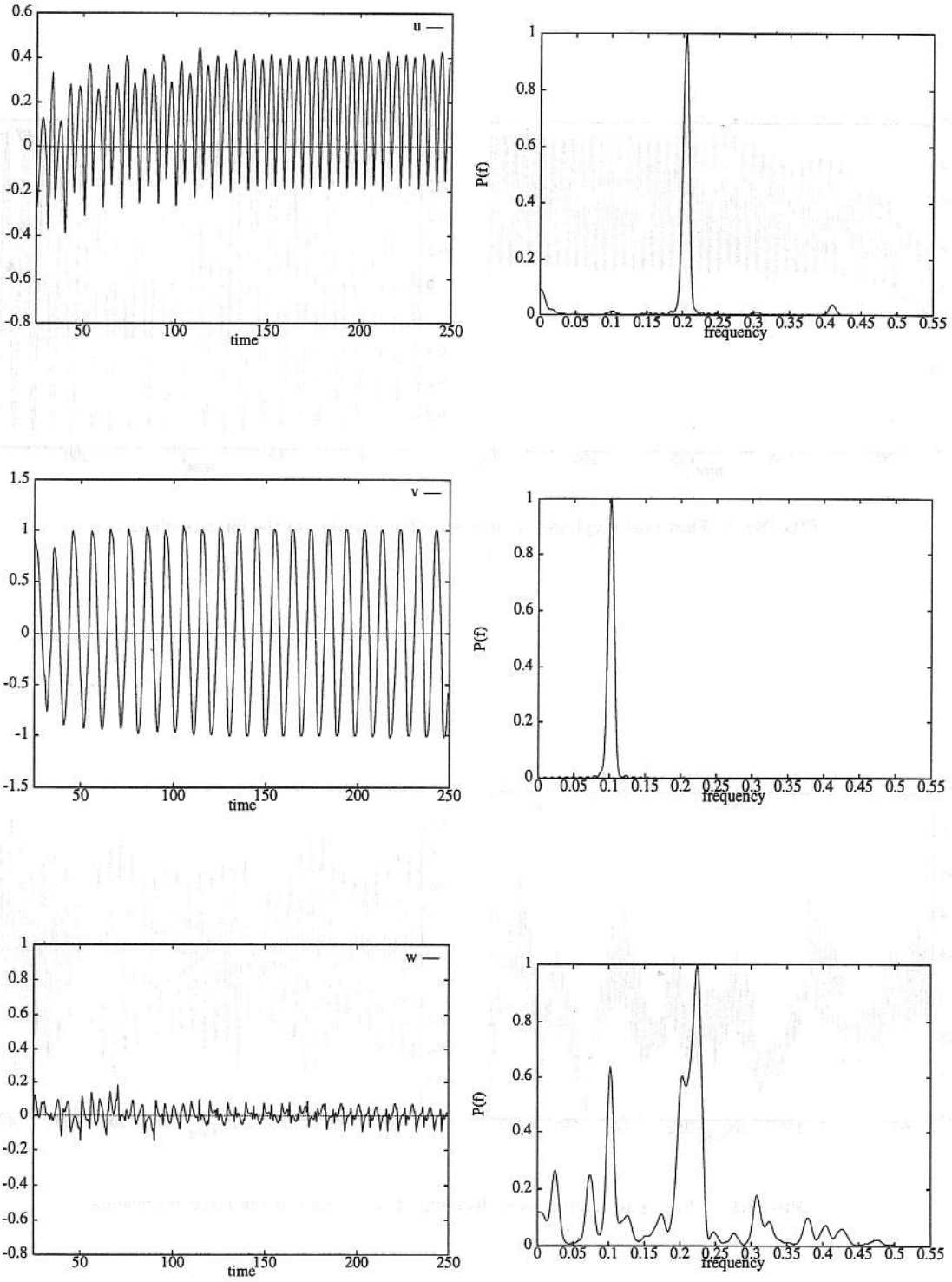

FIGURE 10: Flow past a cylinder at Re=300. Time history and power spectra of 'u', 'v', 'w' at a point located downstream of the cylinder along the centerline.

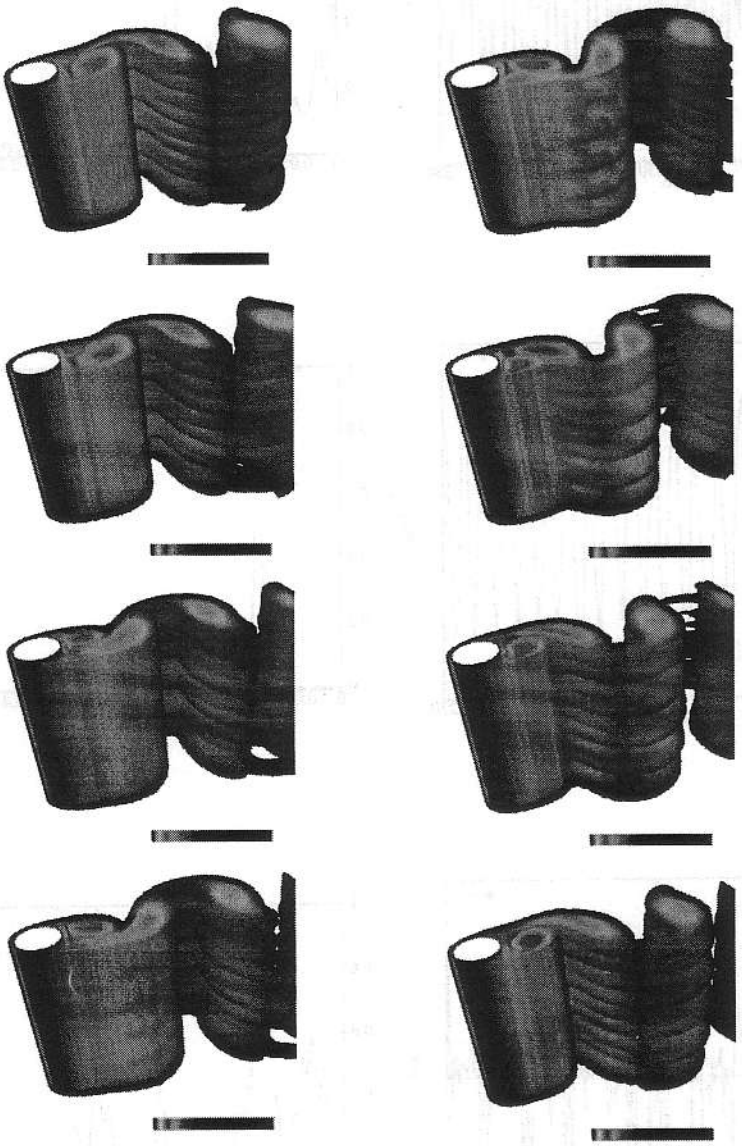

FIGURE 11: Flow past a cylinder at Re=300. Magnitude of the vorticity at different instants (frames 1, 2, 3, 4 on the left and 5, 6, 7, 8 on the right).

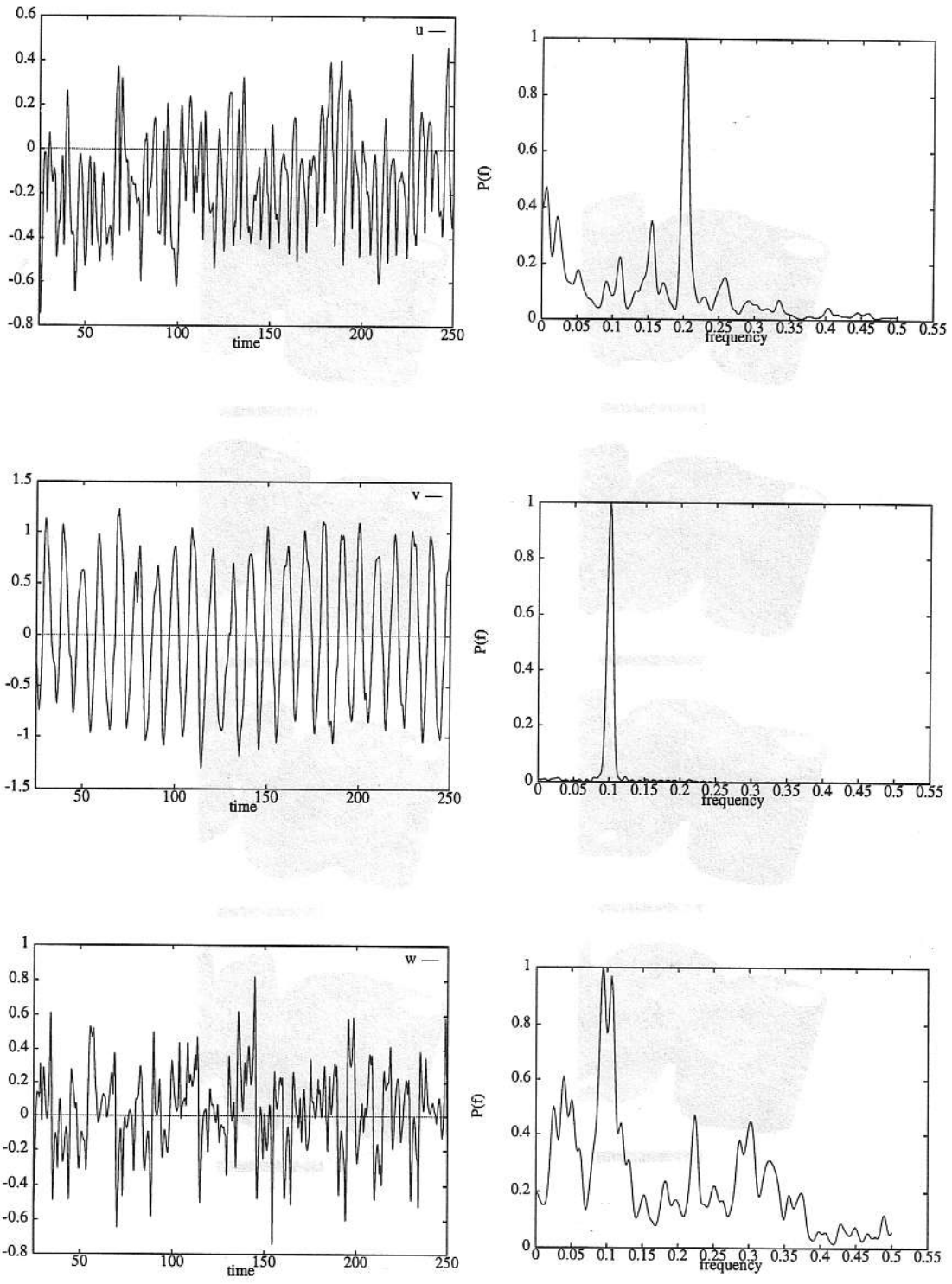

FIGURE 12: Flow past a cylinder at Re=800. Time history and power spectra of 'u', 'v', 'w' at a point located downstream of the cylinder along the centerline.

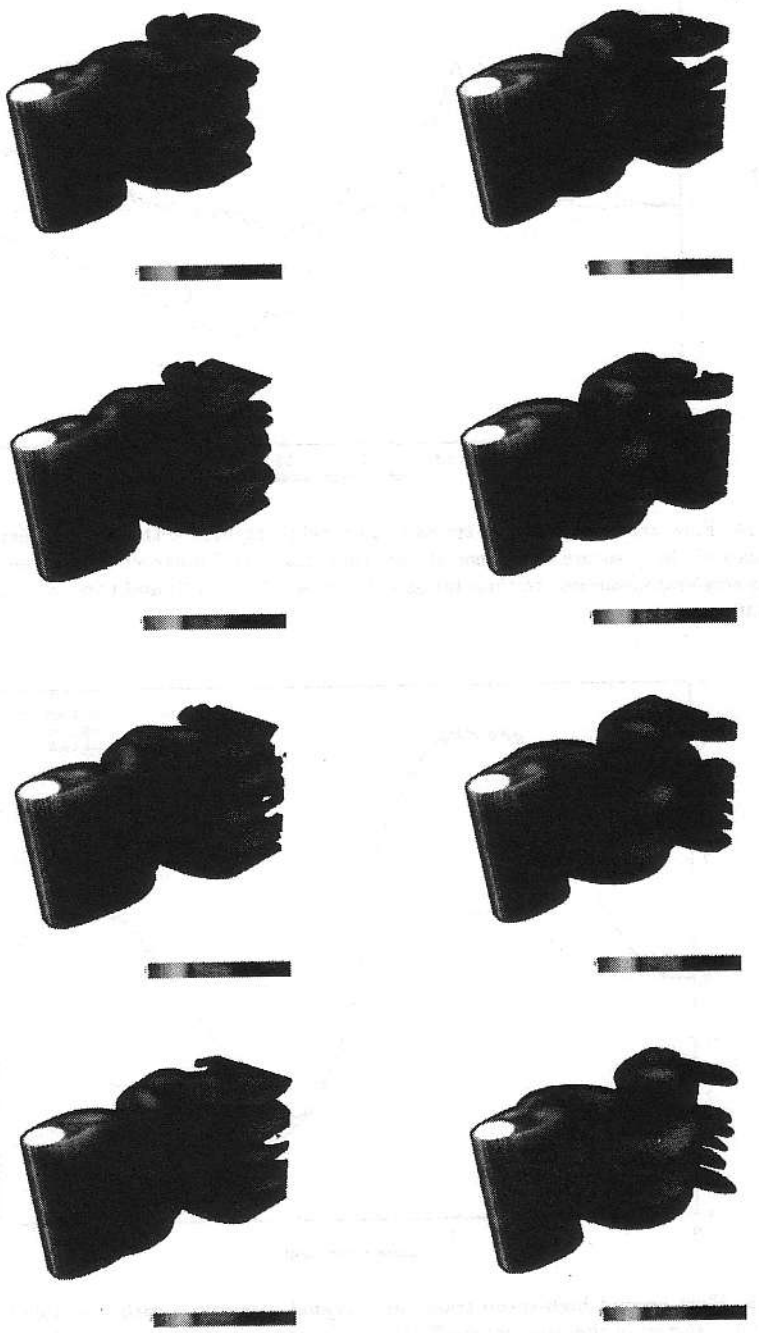

FIGURE 13: Flow past a cylinder at Re=800. Magnitude of the vorticity at different instants (frames 1, 2, 3, 4 on the left and 5, 6, 7, 8 on the right).

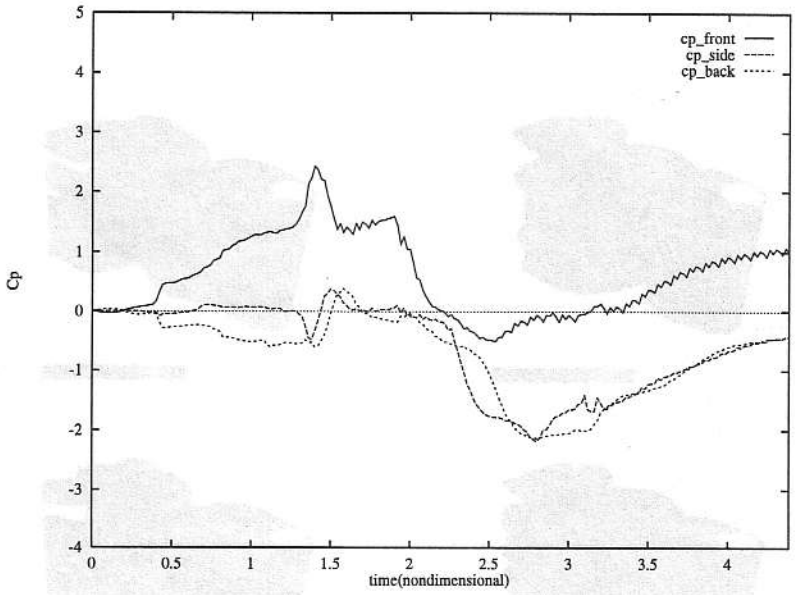

FIGURE 14: Flow around high-speed trains in a tunnel (computed without a turbulence model). Time history of the pressure coefficient at the front, back, and inner side of one of the trains. The trains accelerate from rest to their full speed during $t \in (0.0, 1.0)$ and pass each other during $t \in (2.0, 3.0)$.

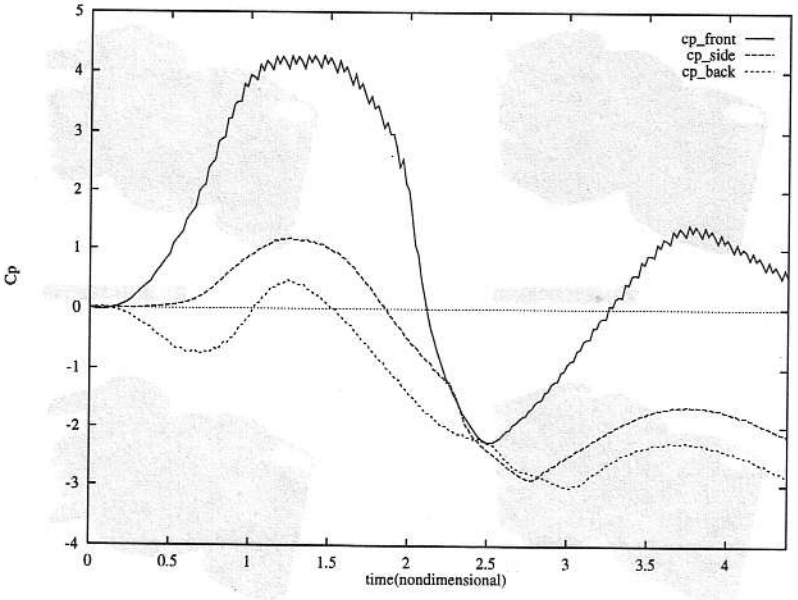

FIGURE 15: Flow around high-speed trains in a tunnel (computed with a simple turbulence model). Time histories of the pressure coefficient at the front, back, and inner side of one of the trains. The trains accelerate from rest to their full speed during $t \in (0.0, 1.0)$ and pass each other during $t \in (2.0, 3.0)$.

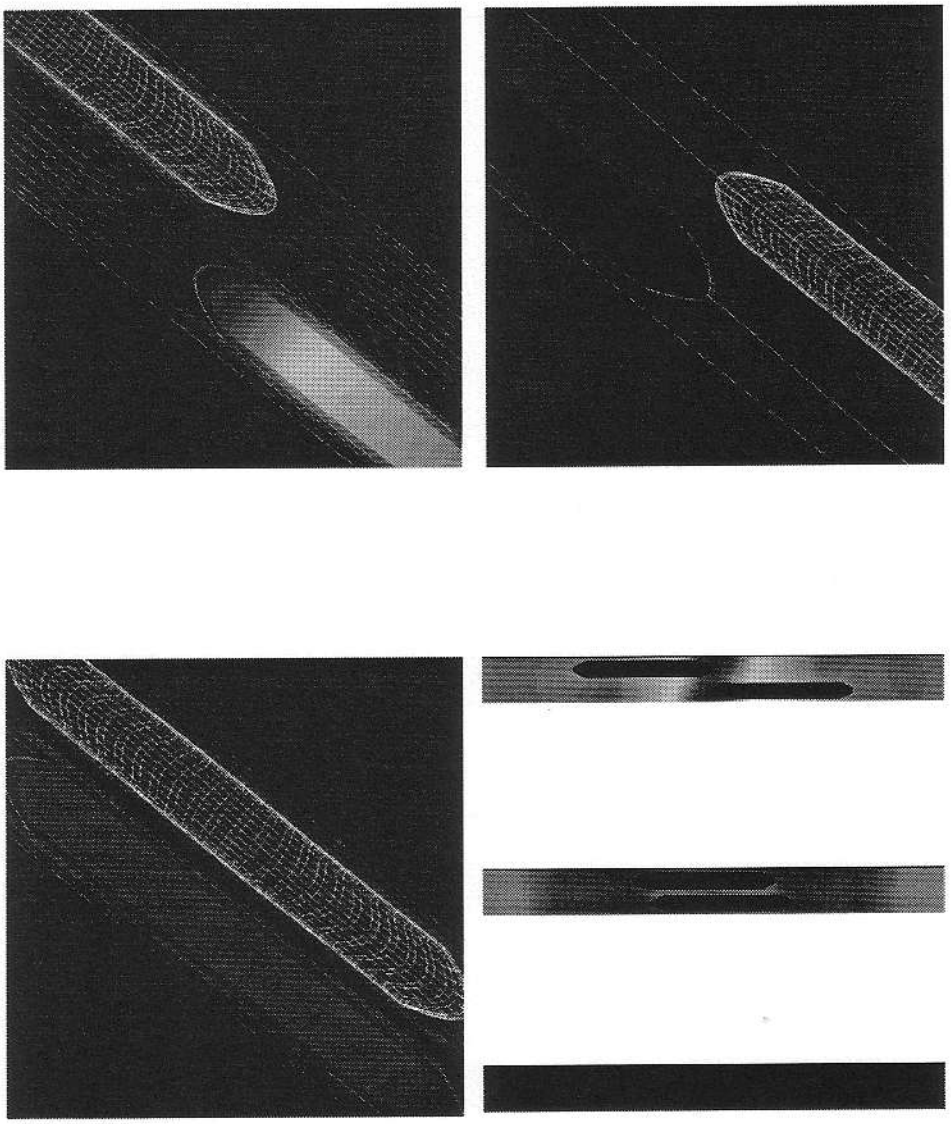

FIGURE 16: Flow around high-speed trains in a tunnel (computed with a simple turbulence model). Surface mesh and pressure field at three different instants. On the bottom right is a 2D section showing the pressure field in the domain.